Structure and magnetism of self-organized Ge$_{1-x}$Mn$_x$ nanocolumns on Ge(001)

T. Devillers,[*] M. Jamet,[†] A. Barski, V. Poydenot, P. Bayle-Guillemaud, and E. Bellet-Amalric
CEA-Grenoble/DSM/DRFMC/SP2M, 17 rue des Martyrs, 38054 Grenoble Cedex 9, France

S. Cherifi and J. Cibert
Institut Néel, CNRS, Boîte Postale 166, 38042 Grenoble Cedex 9, France

We report on the structural and magnetic properties of thin Ge$_{1-x}$Mn$_x$ films grown by molecular beam epitaxy (MBE) on Ge(001) substrates at temperatures (T_g) ranging from 80 to 200 °C, with average Mn content between 1% and 11%. Their crystalline structure, morphology, and composition have been investigated by transmission electron microscopy (TEM), electron energy loss spectroscopy, and x-ray diffraction. In the whole range of growth temperatures and Mn concentrations, we observed the formation of manganese-rich nanostructures embedded in a nearly pure germanium matrix. The growth temperature mostly determines the structural properties of Mn-rich nanostructures. For low growth temperatures (below 120 °C), we evidenced a two-dimensional spinodal decomposition resulting in the formation of vertical one-dimensional nanostructures (nanocolumns). Moreover, we show in this paper the influence of growth parameters (T_g and Mn content) on this decomposition, i.e., on the nanocolumn size and density. For temperatures higher than 180 °C, we observed the formation of Ge$_3$Mn$_5$ clusters. For intermediate growth temperatures, nanocolumns and nanoclusters coexist. Combining high-resolution TEM and superconducting quantum interference device magnetometry, we could evidence at least four different magnetic phases in Ge$_{1-x}$Mn$_x$ films: (i) paramagnetic diluted Mn atoms in the germanium matrix, (ii) superparamagnetic and ferromagnetic low-T_C nanocolumns ($120 \leq T_C \leq 170$ K), (iii) high-T_C nanocolumns ($T_C \geq 400$ K), and (iv) Ge$_3$Mn$_5$ clusters.

I. INTRODUCTION

In the past few years, the synthesis of ferromagnetic semiconductors has become a major challenge for spintronics. Actually, growing a magnetic and semiconducting material could lead to promising advances such as spin injection into nonmagnetic semiconductors, or electrical manipulation of carrier-induced magnetism in magnetic semiconductors.[1,2] Up to now, major efforts have focused on diluted magnetic semiconductors (DMSs) in which the host semiconducting matrix is randomly substituted by transition metal (TM) ions such as Mn, Cr, Ni, Fe, or Co.[3] However, Curie temperatures (T_C) in DMSs remain rather low and TM concentrations must be drastically raised in order to increase T_C up to room temperature. That usually leads to phase separation and the formation of secondary phases. It was recently shown that phase separation induced by spinodal decomposition could lead to a significant increase of T_C.[4,5] For semiconductors showing T_C higher than room temperature, one can foresee the fabrication of nanodevices such as memory nanodots, or nanochannels for spin injection. Therefore, the precise control of inhomogeneities appears as a new challenge which may open a way to industrial applications of ferromagnetism in semiconductors.

The increasing interest in group-IV magnetic semiconductors can also be explained by their potential compatibility with the existing silicon technology. In 2002, carrier-mediated ferromagnetism was reported by Park *et al.*[6] in Ge$_{0.94}$Mn$_{0.06}$ films grown by molecular beam epitaxy (MBE). The maximum critical temperature was 116 K. Recently, many publications indicate a significant increase of T_C in Ge$_{1-x}$Mn$_x$ materials depending on growth conditions.[7–9] Cho

et al. reported a Curie temperature as high as 285 K.[10] Taking into account the strong tendency of Mn ions to form intermetallic compounds in germanium, a detailed investigation of the nanoscale structure is required. Up to now, only a few studies have focused on the nanoscale composition in Ge$_{1-x}$Mn$_x$ films. Local chemical inhomogeneities have been recently reported by Kang *et al.*,[11] who evidenced a micrometer-scale segregation of manganese in large Mn-rich stripes. Ge$_3$Mn$_5$ as well as Ge$_8$Mn$_{11}$ clusters embedded in a germanium matrix have been reported by many authors. However, Curie temperatures never exceed 300 K.[12–15] Ge$_3$Mn$_5$ clusters exhibit a Curie temperature of 296 K.[16] This phase, frequently observed in Ge$_{1-x}$Mn$_x$ films, is the most stable (Ge,Mn) alloy. The other stable compound Ge$_8$Mn$_{11}$ has also been observed in nanocrystallites surrounded with pure germanium.[17] Ge$_8$Mn$_{11}$ and Ge$_3$Mn$_5$ phases are ferromagnetic but their metallic character considerably complicates their potential use as spin injectors. Recently, some new Mn-rich nanostructures have been evidenced in Ge$_{1-x}$Mn$_x$ layers. Sugahara *et al.*[18] reported the formation of high-Mn-content (between 10% and 20% of Mn) amorphous Ge$_{1-x}$Mn$_x$ precipitates in a Mn-free germanium matrix. Mn-rich coherent cubic clusters were observed by Ahlers *et al.*[15] which exhibit a Curie temperature below 200 K. Finally, high-T_C (>400 K) Mn-rich nanocolumns have been evidenced,[19] which could lead to silicon-compatible room-temperature operational devices.

In the present paper, we investigate the structural and magnetic properties of Ge$_{1-x}$Mn$_x$ thin films for low growth temperatures (<200 °C) and low Mn concentrations (between 1% and 11%). By combining transmission electron microscopy (TEM), x-ray diffraction, and superconducting
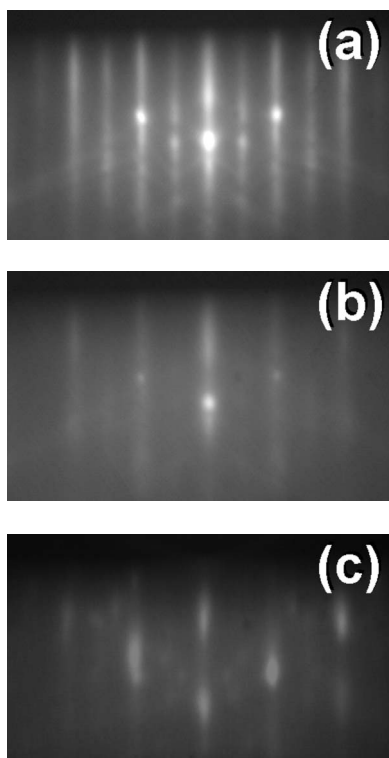
FIG. 1. RHEED patterns recorded during the growth of $Ge_{1-x}Mn_x$ films: (a) 2×1 surface reconstruction of the germanium buffer layer; (b) 1×1 streaky RHEED pattern obtained at low growth temperatures ($T_g < 180$ °C); (c) RHEED pattern of a sample grown at $T_g = 180$ °C. The additional spots reveal the presence of Ge_3Mn_5 clusters at the surface of the film.

quantum interference device (SQUID) magnetometry, we could identify different magnetic phases. We show that, depending on growth conditions, we obtain either Mn-rich nanocolumns or Ge_3Mn_5 clusters embedded in a germanium matrix. We discuss the structural and magnetic properties of these nanostructures as a function of manganese concentration and growth temperature. We also discuss the magnetic anisotropy of nanocolumns and Ge_3Mn_5 clusters.

II. SAMPLE GROWTH

Growth was performed using solid source molecular beam epitaxy by co-depositing Ge and Mn evaporated from standard Knudsen effusion cells. The deposition rate was low (≈ 0.2 Å s^{-1}). Germanium substrates were epiready Ge(001) wafers with a residual *n*-type doping and resistivity of 10^{15} cm^{-3} and 5 Ω cm, respectively. After thermal desorption of the surface oxide, a 40-nm-thick Ge buffer layer was grown at 250 °C, resulting in a 2×1 surface reconstruction as observed by reflection high-energy electron diffraction (RHEED) [see Fig. 1(a)]. Next, 80-nm-thick $Ge_{1-x}Mn_x$ films were subsequently grown at low substrate temperature (from 80 to 200 °C). The Mn content has been determined by x-ray fluorescence measurements performed on thick samples (≈ 1 μm thick) and complementary Rutherford backscattering on thin $Ge_{1-x}Mn_x$ films grown on silicon. The Mn concentrations range from 1% to 11% Mn.

For $Ge_{1-x}Mn_x$ films grown at substrate temperatures below 180 °C, after the first monolayer (ML) deposition, the 2×1 surface reconstruction almost totally disappears. After depositing a few monolayers, a slightly diffuse 1×1 streaky RHEED pattern and a very weak 2×1 reconstruction [Fig. 1(b)] indicate a predominantly two-dimensional growth. For growth temperatures above 180 °C, additional spots appear in the RHEED pattern during the $Ge_{1-x}Mn_x$ growth [Fig. 1(c)]. These spots may correspond to the formation of very small secondary-phase crystallites. The nature of these crystallites will be discussed below.

TEM observations were performed using a JEOL 4000EX microscope with an acceleration voltage of 400 kV. Energy-filtered transmission electron microscopy (EFTEM) was done using a JEOL 3010 microscope equipped with a Gatan image filter. Sample preparation was carried out by standard mechanical polishing and argon ion milling for cross-section investigations, and plane views were prepared by wet etching with H_3PO_4-H_2O_2 solution.[20]

III. STRUCTURAL PROPERTIES

In samples grown at 130 °C and containing 6% Mn, we can observe vertical elongated nanostructures, i.e., nanocol-
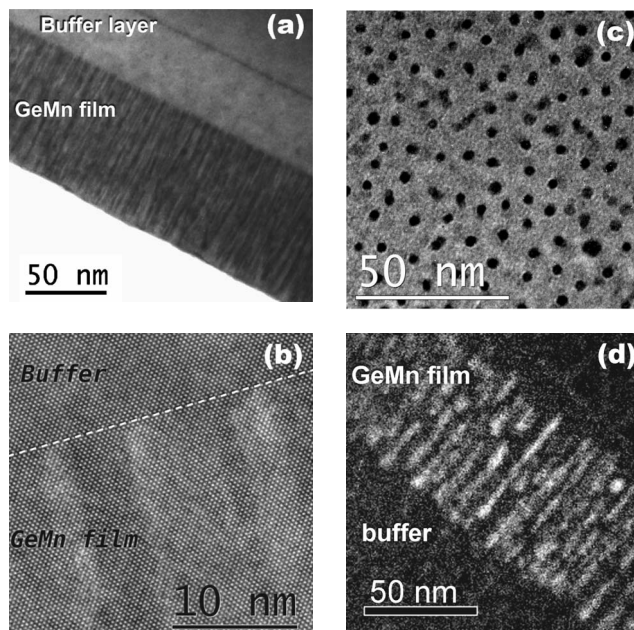
FIG. 2. Transmission electron micrographs of a $Ge_{1-x}Mn_x$ film grown at 130 °C and containing 6% of manganese. (a) Cross section along the [110] axis; we clearly see the presence of nanocolumns elongated along the growth axis. (b) High-resolution image of the interface between the $Ge_{1-x}Mn_x$ film and the Ge buffer layer. The $Ge_{1-x}Mn_x$ film exhibits the same diamond structure as pure germanium. No defect can be seen that could be caused by the presence of nanocolumns. (c) Plane view micrograph performed on the same sample confirms the columnar structure and gives the density and size distribution of nanocolumns. (d) Mn chemical map obtained by energy-filtered transmission electron microscopy. The background was carefully subtracted from preedge images. Bright areas correspond to Mn-rich regions.
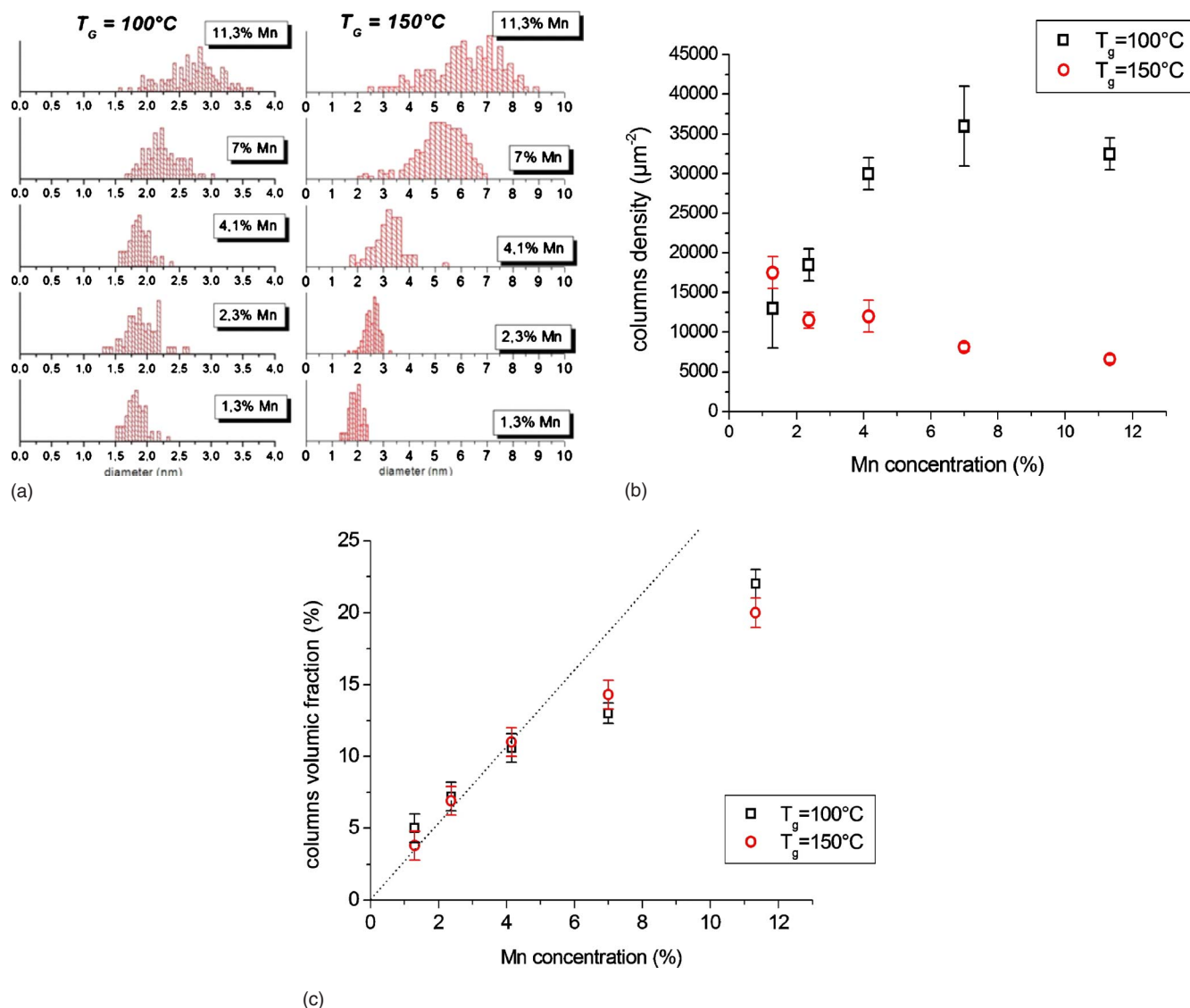
FIG. 3. (Color online) Nanocolumn size and density as a function of growth conditions. Samples considered have been grown at 100 and 150 °C, respectively. (a) Mn concentration dependence of the size distribution. (b) Column density as a function of Mn concentration. (c) Volume fraction of the nanocolumns as a function of Mn concentration.

umns as shown in Fig. 2(a). Nanocolumns extend through the whole $Ge_{1-x}Mn_x$ film thickness. From the high-resolution TEM image shown in Fig. 2(b), we deduce their average diameter around 3 nm. Moreover in Fig. 2(b), the interface between the Ge buffer layer and the $Ge_{1-x}Mn_x$ film is flat, and no defect propagates from the interface into the film. The $Ge_{1-x}Mn_x$ film is a perfect single crystal in epitaxial relationship with the substrate. In Fig. 2(c) is shown a plane view micrograph of the same sample, confirming the presence of nanocolumns in the film. From this image, we can deduce the size and density of nanocolumns. The nanocolumn density is 13 000 μm^{-2} with a mean diameter of 3 nm, which is coherent with cross-section measurements. In order to estimate the chemical composition of these nanocolumns, we further performed chemical mapping using EFTEM. In Fig. 2(d) we show a cross-sectional Mn chemical map of the $Ge_{1-x}Mn_x$ film. This map shows that the formation of nanocolumns is a consequence of Mn segregation. The nanocol-

umns are Mn rich and the surrounding matrix is Mn poor. However, it is impossible to deduce the Mn concentration in $Ge_{1-x}Mn_x$ nanocolumns from this cross section. Indeed, in cross-section observations, the columns diameter is much smaller than the probed film thickness, and the signal comes from the superposition of the Ge matrix and Mn-rich nanocolumns. In order to quantify Mn concentration inside the nanocolumns and inside the Ge matrix, electron energy loss spectroscopy measurements (not shown here) have been performed in a plane view geometry.[19] These observations revealed that the matrix Mn content is below 1% (detection limit of our instrument). By measuring the surface occupied by the matrix and the nanocolumns in plane view TEM images, and considering the average Mn concentration in the sample (6%), we can estimate the Mn concentration in the nanocolumns. The Mn concentration measured by EELS being between 0% and 1%, we can conclude that the Mn content in the nanocolumns is between 30% and 38%.
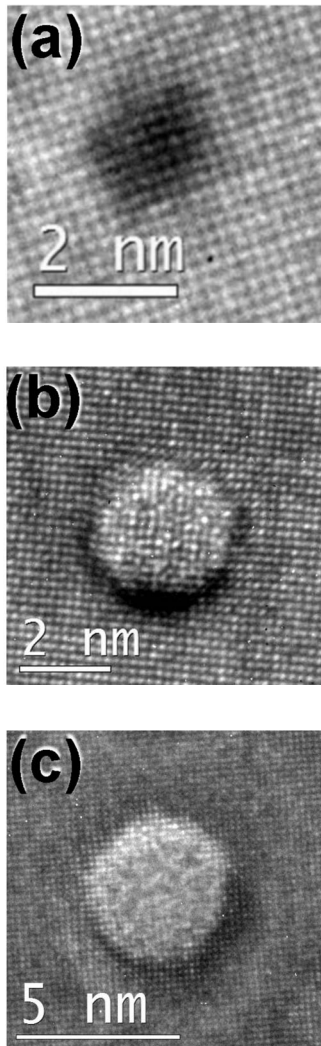
FIG. 4. Plane view high-resolution transmission electron micrographs of different types of nanocolumns. (a) Typical structure of a column grown at 100 °C. The crystal structure is exactly the same as in germanium. (b) Partially relaxed nanocolumn. One can see dislocations at the interface between the columns and the matrix leading to stress relaxation. (c) Amorphous nanocolumn. These columns are typical in samples grown at 150 °C with high Mn content.

For samples grown between 80 and 150 °C, cross-section and plane view TEM observations reveal the presence of Mn-rich nanocolumns surrounded with a Mn-poor Ge matrix. In order to investigate the influence of Mn concentration on the structural properties of $Ge_{1-x}Mn_x$ films, ten samples were grown at 100 and at 150 °C with Mn concentrations of 1.3%, 2.3%, 4%, 7%, and 11.3%. Their structural properties have been investigated by plane view TEM observations. For samples grown at 100 °C with Mn concentrations below 5% the nanocolumn mean diameter is 1.8 ± 0.2 nm. The evolution of columns density as a function of Mn concentration is reported in Fig. 3(b). By increasing the Mn concentration from 1.3% to 4%, we observe a significant increase of the column density from 13 000 to 30 000 μm^{-2}. For Mn concentrations higher than 5%, the density seems to reach a plateau corresponding to 35 000 μm^{-2} and their diameter slightly increases from 1.8 nm at 4% to 2.8 nm at 11.3%. By
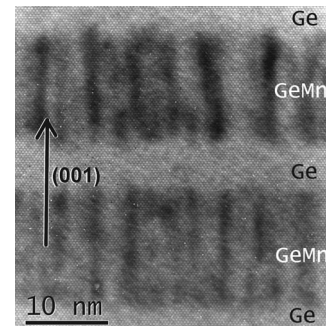
FIG. 5. Cross-section high-resolution micrograph of a $Ge/Ge_{1-x}Mn_x/Ge/Ge_{1-x}Mn_x/Ge$ heterostructure. This sample was grown at 130 °C with 6% Mn. $Ge_{1-x}Mn_x$ layers are 15 nm thick and Ge spacers 5 nm thick. We clearly see the sharpness of both $Ge_{1-x}Mn_x/Ge$ and $Ge/Ge_{1-x}Mn_x$ interfaces. Mn segregation leading to column formation already takes place in very thin $Ge_{1-x}Mn_x$ films.

plotting the volume fraction occupied by the columns in the film as a function of Mn concentration, we observe a linear dependence for Mn content below 5%. The nonlinear behavior above 5% may indicate that the mechanism of Mn incorporation is different in this concentration range, leading to an increase of Mn concentration in the columns or in the matrix. For samples grown at 100 °C, the nanocolumns are always fully coherent with the surrounding matrix [Fig. 4(a)].

Increasing the Mn content in the samples grown at 150 °C from 1.3% to 11.3% leads to a decrease of the column density [Fig. 3(b)]. Moreover, their average diameter increases significantly and size distributions become very broad [see Fig. 3(a)]. For the highest Mn concentration (11.3%), we observe the coexistence of very small columns with a diameter of 2.5 nm and very large columns with a diameter of 9 nm. In samples grown at 150 °C containing 11.3% of Mn, the crystalline structure of the nanocolumns is also highly modified. In plane view TEM micrographs, one can see columns exhibiting several different crystalline structures. We still observe some columns that are fully coherent with the Ge matrix as in the samples grown at lower temperature. Nevertheless, observations performed on these samples grown at 150 °C and with 11.3% Mn reveal some
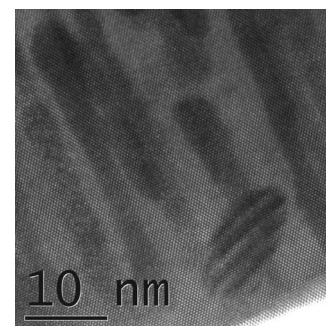
FIG. 6. Cross-section high-resolution transmission electron micrograph of a sample grown at 170 °C. We observe the coexistence of two different Mn-rich phases: $Ge_{1-x}Mn_x$ nanocolumns and Ge_3Mn_5 clusters.

uniaxially[19] or fully relaxed columns exhibiting a misfit of 4% between the matrix and the columns, and leading to misfit dislocations at the interface between the column and the matrix [see Fig. 4(b)]. Thus we can conclude that coherent columns are probably in strong compression and the surrounding matrix in tension. On the same samples (T_g =150 °C, 11.3% Mn), we also observe a large number of highly disordered nanocolumns, leading to an amorphouslike TEM contrast [Fig. 4(c)].

In conclusion, we have evidenced a complex mechanism of Mn incorporation in Mn-doped Ge films grown at low temperature. In particular, Mn incorporation is highly inhomogeneous. For very low growth temperatures (below 120 °C), the diffusion of Mn atoms leads to the formation of Mn-rich vertical nanocolumns. Their density mostly depends on Mn concentration and their mean diameter is about 2 nm. These results can be compared with the theoretical predictions of Fukushima et al.:[5] they proposed a model of spinodal decomposition in $(Ga,Mn)N$ and $(Zn,Cr)Te$ based on layer-by-layer growth conditions and a strong pairing attraction between Mn atoms, which leads to the formation of nanocolumns. This model may also properly describe the formation of Mn-rich nanocolumns in our samples. Layer-by-layer growth conditions can be deduced from RHEED pattern evolution during growth. For all the samples grown at low temperature, the RHEED observations clearly indicate two-dimensional growth. Moreover, $Ge/Ge_{1-x}Mn_x/Ge$ heterostructures have been grown and observed by TEM (see Fig. 5). $Ge_{1-x}Mn_x/Ge$ (as well as $Ge/Ge_{1-x}Mn_x$) interfaces are very flat and sharp, thus confirming a two-dimensional layer-by-layer growth mode. Therefore we can assume that the formation of Mn-rich nanocolumns is a consequence of two-dimensional (2D) spinodal decomposition.

For growth temperatures higher than 160 °C, cross-section TEM and EFTEM observations (not shown here) reveal the coexistence of two Mn-rich phases: nanocolumns and Ge_3Mn_5 nanoclusters embedded in the germanium matrix. A typical high-resolution TEM image is shown in Fig. 6. Ge_3Mn_5 clusters are not visible in RHEED patterns for temperatures below 180 °C. To investigate the nature of these clusters, we performed x-ray diffraction in θ-2θ mode. Diffraction scans were acquired on a high-resolution diffractometer using the copper $K\alpha$ radiation and on the GMT station of the BM32 beamline at the European Synchrotron Radiation Facility (ESRF). Three samples grown at different temperatures and/or annealed at high temperature were investigated. The two first samples are $Ge_{1-x}Mn_x$ films grown at 130 and 170 °C, respectively. The third one was grown at 130 °C and postgrowth annealed at 650 °C. By analyzing the x-ray diffraction spectra, we can evidence two different crystalline structures. For the sample grown at 130 °C, the θ-2θ scan reveals only the (004) Bragg peak of the germanium crystal, confirming the good epitaxial relationship between the layer and the substrate, and the absence of secondary phases in the film in spite of a high dynamics of the order of 10^7. For both samples grown at 170 °C and annealed at 650 °C, θ-2θ spectra are identical. In addition to the (004) peak of germanium, we observe three additional weak peaks. The first one corresponds to the (002) germanium forbidden peak, which probably comes from a small distortion of the

germanium crystal, and the two other peaks are attributed to the (002) and (004) Bragg peaks of a secondary phase. The c lattice parameter of the Ge_3Mn_5 hexagonal crystal is 5.053 Å,[21] which is in very good agreement with the values obtained from diffraction data for both (002) and (004) lines, assuming that the c axis of Ge_3Mn_5 is along the [001] direction of the Ge substrate.

In summary, in a wide range of growth temperatures and Mn concentrations, we have evidenced a two-dimensional spinodal decomposition leading to the formation of Mn-rich nanocolumns in $Ge_{1-x}Mn_x$ films. This decomposition is probably the consequence of (i) a strong pairing attraction between Mn atoms, (ii) a strong surface diffusion of Mn atoms in germanium even at low growth temperatures, and (iii) layer-by-layer growth conditions. We have also investigated the influence of growth parameters on the spinodal decomposition: at low growth temperatures (100 °C), increasing the Mn content leads to higher column densities, while at higher growth temperatures (150 °C), the column density remains nearly constant, whereas their size increases drastically. By plotting the nanocolumn density as a function of Mn content, we have shown that the mechanism of Mn incorporation in Ge changes above 5% of Mn. Finally, using TEM observations and x-ray diffraction, we have shown that Ge_3Mn_5 nanoclusters start to form at growth temperatures higher than 160 °C.

IV. MAGNETIC PROPERTIES

We have thoroughly investigated the magnetic properties of thin $Ge_{1-x}Mn_x$ films for different growth temperatures and Mn concentrations. In this section, we focus on Mn concen-
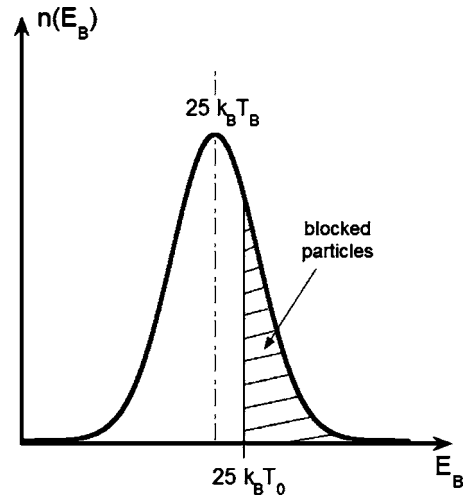
FIG. 7. Schematic drawing of the anisotropy barrier distribution $n(E_B)$ of superparamagnetic nanostructures. If magnetic anisotropy does not depend on the nanostructure size, this distribution exactly reflects the magnetic size distribution. In this drawing the blocking temperature (T_B) corresponds to the distribution maximum. At a given temperature T_0 such that $25k_BT_0$ falls into the anisotropy barrier distribution, the largest nanostructures with an anisotropy energy larger than $25k_BT_0$ are blocked, whereas the others are superparamagnetic.
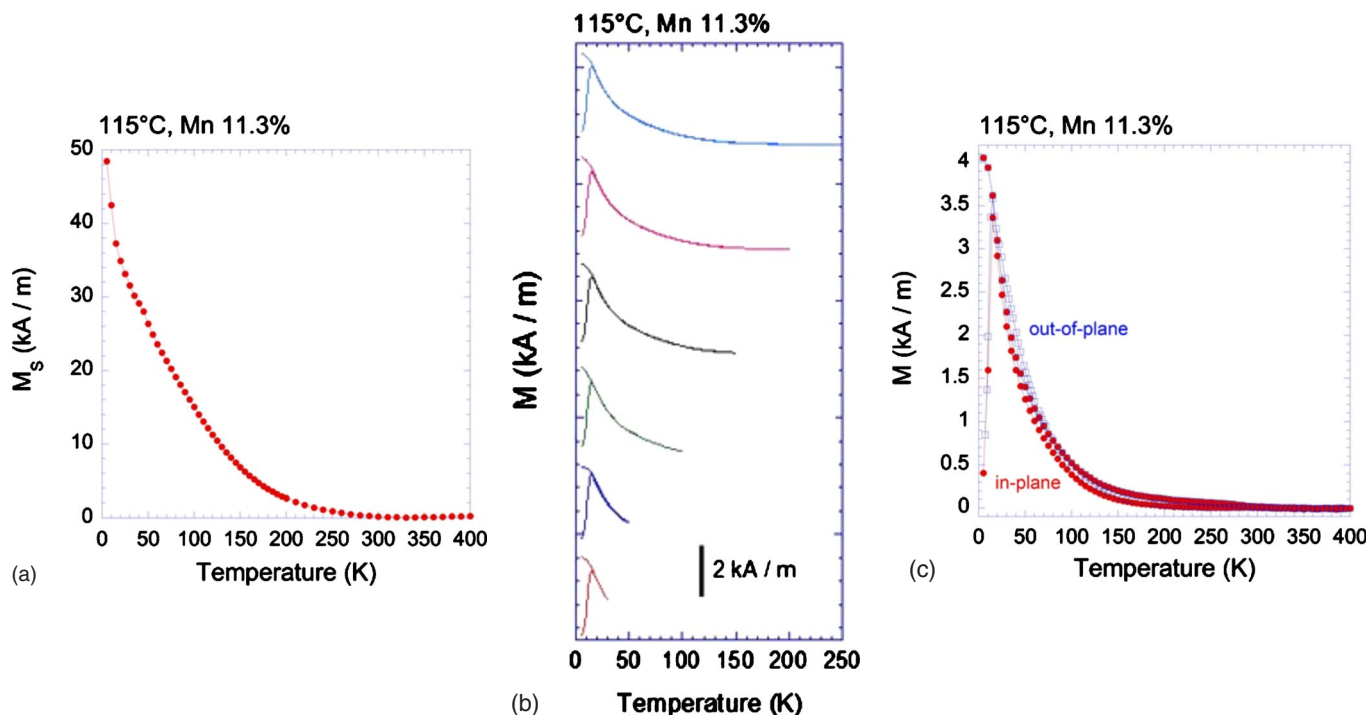
FIG. 8. (Color online) (a) Temperature dependence of the saturation magnetization of a $Ge_{0.89}Mn_{0.11}$ sample grown at 115 °C. The applied field is 2 T. (b) ZFC-FC measurements. The in-plane applied field is 0.015 T. Magnetization was recorded up to different T_0 temperatures: 30, 50, 100, 150, 200, and 250 K. Curves are shifted up for more clarity. (c) ZFC-FC curves for in-plane (red dots) and out-of-plane (open blue squares) applied fields (0.015 T).

trations between 2% and 11%. We could clearly identify four different magnetic phases in $Ge_{1-x}Mn_x$ films: diluted Mn atoms in the germanium matrix, low-T_C nanocolumns ($T_C \leq 170$ K), high-T_C nanocolumns ($T_C \geq 400$ K), and Ge_3Mn_5 clusters ($T_C \approx 300$ K). The relative weight of each phase clearly depends on the growth temperature and to a lesser extent on Mn concentration. Hence, in the next three sections, we detail the magnetic properties of $Ge_{1-x}Mn_x$ films grown at different growth temperatures: (i) $T_g \leq 120$ °C, (ii) $120 < T_g < 145$ °C, and (iii) $T_g \geq 145$ °C. Moreover, for the first and last regimes, we have studied the influence of Mn concentration. We have carried out saturation magnetization measurements in order to detect all the magnetic phases present in the sample and estimate their Curie temperature. Then zero-field-cooled–field-cooled (ZFC-FC) measurements were performed to detect superparamagnetic nanostructures, estimate their blocking temperature (T_B), and probe their anisotropy barrier distribution. The blocking temperature is defined as the temperature above which a ferromagnetic nanostructure becomes superparamagnetic, i.e., the measuring time is comparable to the relaxation time of its magnetization. In the ZFC-FC procedure, the sample is first cooled down to 5 K in zero magnetic field and the magnetic moment is subsequently recorded at low field while increasing the temperature up to a temperature $T_0 \leq 400$ K (ZFC curve). Then the magnetic moment is recorded under the same magnetic field while decreasing the temperature down to 5 K (FC curve). If T_0 falls into the anisotropy barrier distribution or above, as depicted in Fig. 7, the FC curve deviates from the ZFC curve. Indeed, the smallest nanostruc-

tures have become superparamagnetic at T_0 and when the temperature is decreased again, their magnetization freezes along a direction close to the magnetic field and the FC magnetic moment becomes larger than the ZFC one. Therefore any irreversibility in this procedure points at the presence of superparamagnetic nanostructures. Because the applied magnetic field is weak, ZFC-FC measurements are also called susceptibility measurements in the following. At this stage, we have to mention that Ge_3Mn_5 nanoclusters are detected by SQUID at lower growth temperatures (down to 120 °C) than is expected from TEM or x-ray diffraction. SQUID measurements are indeed very sensitive to the presence of magnetic nanoclusters.

A. $T_g \leq 120$ °C

For $T_g \leq 120$ °C, the temperature dependence of the saturation magnetization is displayed in Fig. 8(a) and remains nearly the same on increasing growth temperature. The vanishing of the overall magnetic signal above 200 K is attributed to the nanocolumns, whereas the increasing signal below 50 K originates from diluted Mn atoms in the surrounding matrix. ZFC-FC measurements show that the nanocolumns are superparamagnetic. The magnetic signal from the diluted Mn atoms in the matrix is too weak to be detected in susceptibility measurements at low temperature. The ZFC curves shown in Figs. 8(b) and 8(c) exhibit a very narrow peak with a maximum at the blocking temperature of 15 K. Therefore the anisotropy barrier distribution is narrow and, assuming that the nanocolumns have the same magnetic
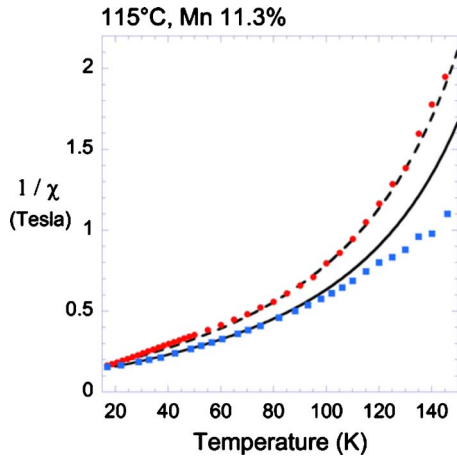
FIG. 9. (Color online) Temperature dependence of the inverse in-plane (red circles) and out-of-plane (blue squares) normalized susceptibilities of a $Ge_{0.89}Mn_{0.11}$ sample grown at 115 °C. Fits were performed assuming isotropic nanostructures or cubic anisotropy. Dashed line is for in-plane susceptibility and solid line for out-of-plane susceptibility.

FIG. 10. (Color online) Temperature dependence of the saturation magnetization (in μ_B/Mn) of $Ge_{1-x}Mn_x$ films grown at 100 °C plotted for different Mn concentrations 4.1, 7, 8.9, and 11.3%.

anisotropy, this is a consequence of the very narrow size distribution of the nanocolumns as observed by TEM. We have also carried out ZFC-FC measurements at different T_0 temperatures. The results are given in Fig. 8(b). ZFC and FC curves clearly superimpose up to $T_0 = 250$ K; thus the nanocolumns are superparamagnetic up to their Curie temperatures and no Ge_3Mn_5 clusters could be detected. Moreover, for low T_0 values, a peak appears at low temperature in the FC curves, which evidences strong antiferromagnetic interactions between the nanocolumns.[22] Indeed, in the temperature range corresponding to the ZFC peak, the FC curve of noninteracting nanostructures should increase on decreasing the temperature, because more and more particles become ferromagnetic. Then the FC curve exhibits a plateau below the corresponding ZFC peak. However, in $Ge_{1-x}Mn_x$ films, for low T_0 values, FC curves exhibit a peak, meaning that the nanocolumn system freezes into a zero-magnetization state due to antiferromagnetic couplings that are not compensated by the applied field.

In order to derive the magnetic size and anisotropy of the Mn-rich nanocolumns embedded in the Ge matrix, we have fitted the inverse normalized in-plane (out-of-plane) susceptibility $\chi_{\parallel}^{-1}$ ($\chi_{\perp}^{-1}$). The corresponding experimental ZFC-FC curves are reported in Fig. 8(c). Since susceptibility measurements are performed at low field (0.015 T), the matrix magnetic signal remains negligible. In order to normalize the susceptibility data, we need to divide the magnetic moment by the saturated magnetic moment recorded at 5 T. However, the matrix magnetic signal becomes very strong at 5 T and low temperature, so that we need to subtract it from the saturated magnetic moment using a simple Curie function. From Fig. 8(c), we can conclude that the nanocolumns are isotropic. Therefore to fit the experimental data we use the following expression, well suited for isotropic systems or cubic anisotropy: $\chi_{\parallel}^{-1} = \chi_{\perp}^{-1} \approx 3k_BT/M(T) + \mu_0 H_{eff}(T)$. k_B is the Boltzmann constant, and $M = M_s v$ is the magnetic mo-

ment of a single-domain nanostructure (macrospin approximation) where M_s is its magnetization and v its volume. The in-plane magnetic field is applied along the [110] or [$\bar{1}$10] crystal axis. Since the nanostructure Curie temperature does not exceed 170 K, the temperature dependence of the saturation magnetization is also accounted for by writing $M(T)$. Antiferromagnetic interactions between nanostructures are also considered by adding an effective field estimated in the mean field approximation:[23] $\mu_0 H_{eff}(T)$. The only fitting parameters are the maximum magnetic moment (i.e., the value at low temperature) per nanostructure M (in Bohr magnetons μ_B) and the maximum interaction field (i.e., at low temperature) $\mu_0 H_{eff}$. In Fig. 9, the best fits lead to $M \approx 1250\mu_B$ and $\mu_0 H_{eff} \approx 102$ mT for in-plane susceptibility and $M \approx 1600\mu_B$ and $\mu_0 H_{eff} \approx 98$ mT for out-of-plane susceptibility. This gives an average magnetic moment of $1425\mu_B$ per column and an effective interaction field of 100 mT. Using this magnetic moment and its temperature dependence, the magnetization curves could be fitted using a Langevin function, and the $M(H/T)$ curves superimpose for $T < 100$ K. However, using the sample magnetic moment at saturation recorded at 2 T and the number of nanocolumns (from the sample area and the column density derived from TEM observation), we can easily calculate the magnetic moment per nanocolumn. We find $6000\mu_B$ per column, which is much larger than the superparamagnetic size of $1425\mu_B$ derived from susceptibility fits. Therefore, for low growth temperatures, we need to assume that the nanocolumns are actually made of almost four independent elongated magnetic nanostructures. The effective field for antiferromagnetic interactions between nanostructures estimated from the susceptibility fits is at least one order of magnitude larger than what is expected from pure magnetostatic coupling. This difference may be due either to an additional antiferromagnetic coupling through the matrix whose origin remains unexplained or to the mean-field approximation which is no longer valid in this strong-coupling regime. As for magnetic anisotropy, the nanostructures behave as isotropic magnetic systems or
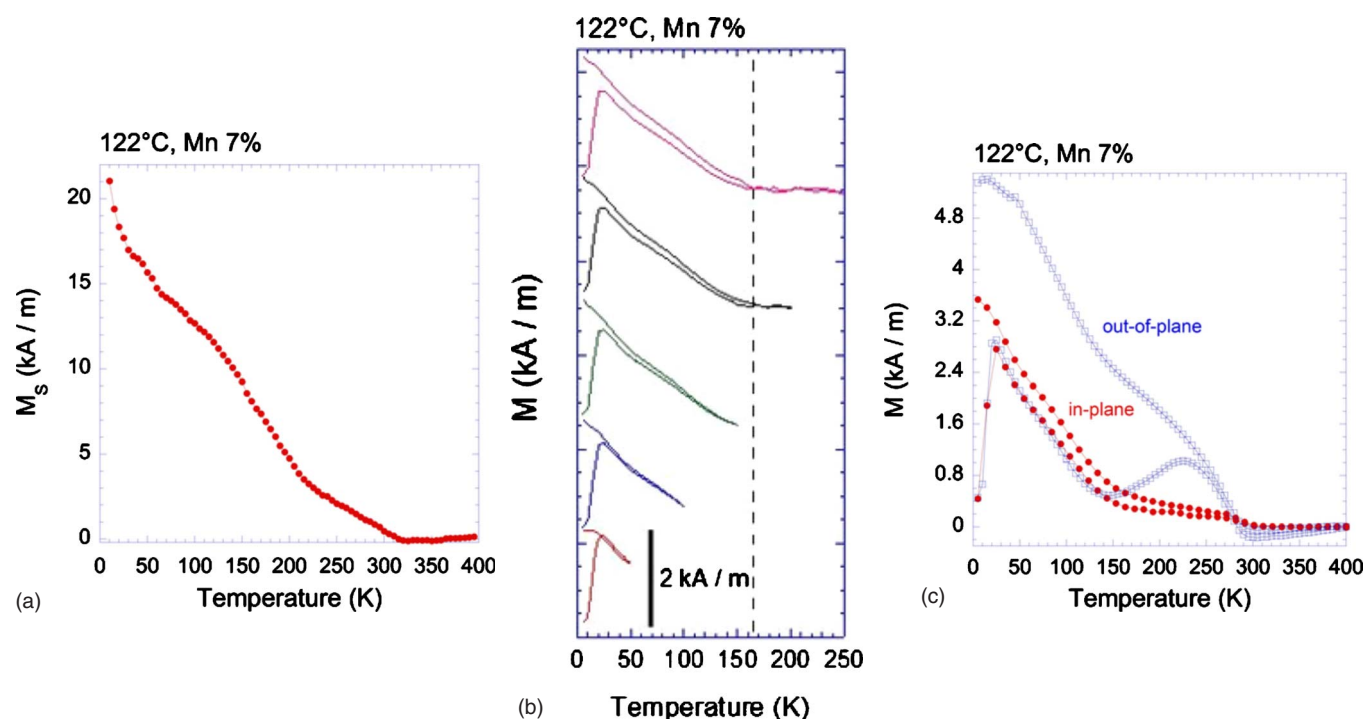
FIG. 11. (Color online) (a) Temperature dependence of the saturation magnetization of a $Ge_{0.93}Mn_{0.07}$ sample grown at 122 °C. The applied field is 2 T. (b) ZFC-FC measurements. The in-plane applied field is 0.015 T. Magnetization was recorded up to different T_0 temperatures: 50, 100, 150, 200, and 250 K. Curves are shifted up for more clarity. (c) ZFC-FC curves for in-plane (red dots) and out-of-plane (open blue squares) applied fields (0.015 T).

exhibit a cubic magnetic anisotropy. First, we can confirm that nanostructures are not amorphous, otherwise the shape anisotropy would dominate, leading to out-of-plane anisotropy. We can also rule out a random distribution of magnetic easy axes, since the nanostructures are clearly crystallized in the diamond structure and will exhibit at least a cubic anisotropy (unless the random distribution of Mn atoms within the nanostructures can yield random easy axes). Since the nanostructures are in strong in-plane compression (their lattice parameter is larger than that of the matrix), the cubic symmetry of the diamond structure is broken and magnetic cubic anisotropy is thus unlikely. We rather believe that out-of-plane shape anisotropy is nearly compensated by in-plane magnetoelastic anisotropy due to compression, leading to a pseudocubic anisotropy. From the blocking temperature (15 K) and the magnetic volume of the nanostructures, we can derive the magnetic anisotropy constant using $Kv = 25k_B T_B$: $K \approx 10$ kJ m^{-3}, which is of the same order of magnitude as the shape anisotropy.

Finally, we studied the Mn concentration dependence of the saturation magnetization (Fig. 10). For the lowest Mn concentration (4%), the contribution from diluted Mn atoms is very high and drops sharply for higher Mn concentrations (7%, 9%, and 11.3%). Therefore the fraction of Mn atoms in the diluted matrix decreases with increasing, Mn concentration, probably because the Mn atoms are more and more incorporated in the nanocolumns. In parallel, the Curie temperature of the nanocolumns increases with the Mn concentration, reaching 170 K for 11.3% of Mn. This behavior may be related to different Mn compositions and to the increasing diameter of the nanocolumns (from 1.8 to 2.8 nm) as dis-

cussed in Sec. III. In samples containing 4% of Mn, ZFC and FC curves (not shown) superimpose down to low temperatures. As we do not observe hysteresis loops at low temperature, we believe that at this Mn concentration the nanocolumns are superparamagnetic in the whole temperature range, and the blocking temperature cannot be measured. For higher Mn content, the ZFC curve exhibits a very narrow peak with a maximum at the blocking temperature of 15 K whatever the Mn concentration and growth temperature [see Figs. 8(b) and 8(c)].

B. $120 < T_g < 145$ °C

For growth temperatures $T_g > 120$ °C and Mn concentrations $\geq 7\%$, samples exhibit a magnetic signal above 200 K corresponding to Ge_3Mn_5 clusters [see Fig. 11(a)]. As we can see, SQUID measurements are much more sensitive to the presence of Ge_3Mn_5 clusters, even at low concentration, than the TEM and x-ray diffraction used in Sec. III. We also observe a sharp transition in the ZFC curve [Figs. 11(b) and 11(c)]: the peak becomes very large and is shifted toward high blocking temperatures (the signal is maximum at $T = 23$ K). This can be easily understood as a magnetic percolation of the four independent nanostructures obtained at low growth temperatures into a single magnetic nanocolumn. Therefore the magnetic volume increases sharply as well as the blocking temperatures. At the same time, the size distribution widens as observed in TEM. In Fig. 11(b), we have performed ZFC-FC measurements at different T_0 temperatures. ZFC-FC irreversibility is observed up to the Curie temperature of ≈ 120 K meaning that a fraction of nanocol-

umns is ferromagnetic (i.e., $T_B \geq T_C$). In Fig. 11(c), in-plane and out-of-plane ZFC curves nearly superimpose for $T \leq 150$ K due to the isotropic magnetic behavior of the nanocolumns: in-plane magnetoelastic anisotropy is still compensating for out-of-plane shape anisotropy. Moreover, the magnetic signal above 150 K corresponding to Ge_3Mn_5 clusters that start to form in this growth temperature range is strongly anisotropic. This perpendicular anisotropy confirms the epitaxial relation: $(0002)Ge_3Mn_5 \| (002)Ge$ discussed in Ref. 12. The magnetic easy axis of the clusters lies along the hexagonal c axis, which is perpendicular to the film plane.

In a very narrow temperature range around $T_g = 130$ °C, the nanocolumns exhibit high-T_C (≥ 400 K) ferromagnetism as shown in Fig. 12(a). Moreover, ZFC-FC measurements in Fig. 12(b) rule out the presence of superparamagnetic nanostructures in the samples. The magnetic properties of these high-T_C nanocolumns are discussed in detail in Ref. 19.

C. $T_g \geq 145$ °C

For growth temperatures $T_g \geq 145$ °C the Ge_3Mn_5 cluster magnetic signal dominates [Figs. 13(a) and 13(c)]. Superparamagnetic nanostructures are investigated by performing ZFC-FC measurements at different T_0 temperatures [Fig. 13(b)]. The first ZFC peak at low temperature, i.e., ≤ 150 K, is attributed to low-T_C nanocolumns ($T_C \approx 130$ K). This peak is wider than for lower growth temperatures and its maximum is further shifted up to 30 K. These results are in agreement with TEM observations: increasing T_g leads to larger nanocolumns (i.e., higher blocking temperatures) and wider size distributions. ZFC-FC irreversibility is observed up to the Curie temperature due to the presence of ferromagnetic columns. The second peak above 180 K in the ZFC curve is attributed to Ge_3Mn_5 clusters, and the corresponding ZFC-FC irreversibility persisting up to 300 K means that some clusters are ferromagnetic. We clearly evidence the out-of-plane anisotropy of Ge_3Mn_5 clusters and the isotropic magnetic behavior of nanocolumns [Fig. 13(c)].

In this growth temperature range, we have also investigated the Mn concentration dependence of magnetic properties. In Fig. 14(a), for low Mn concentrations (2.3% and 4%) the contribution from diluted Mn atoms in the germanium matrix to the saturation magnetization is very high and nearly vanishes for higher Mn concentrations (7%, 9%, and 13%) as observed for low growth temperatures. Above 7%, the magnetic signal mainly comes from nanocolumns and Ge_3Mn_5 clusters. We can derive more information from ZFC-FC measurements [Fig. 14(b)]. Indeed, for 2.3% of Mn, the ZFC and FC curves nearly superimpose down to low temperature, meaning that the nanocolumns are superparamagnetic in the whole temperature range. Moreover, the weak irreversibility arising at 300 K means that some Ge_3Mn_5 clusters have already formed in the samples even at very low Mn concentrations. For 4% of Mn, we can observe a peak with a maximum at the blocking temperature (12 K) in the ZFC curve. We can also derive the Curie temperature of nanocolumns: ≈ 45 K. The irreversibility arising at 300 K still comes from Ge_3Mn_5 clusters. Increasing the Mn concentration above 7% leads to higher blocking temperatures (20
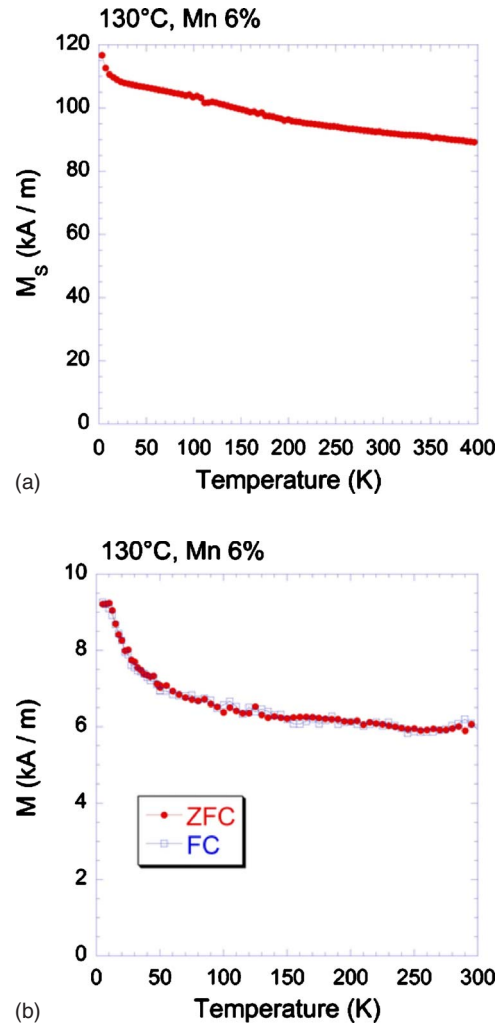
FIG. 12. (Color online) (a) Temperature dependence of the saturation magnetization of a $Ge_{0.94}Mn_{0.06}$ sample grown at 130 °C. The applied field is 2 T. (b) ZFC-FC measurements. The in-plane applied field is 0.01 T.

and 30 K) due to larger nanocolumns and wider ZFC peaks due to wider size distributions, in agreement with TEM observations [see Fig. 3(a)]. Curie temperatures also increase (110 and 130 K), as well as the contribution from Ge_3Mn_5 clusters.

Finally, on increasing T_g above 160 °C, the nanocolumn magnetic signal nearly vanishes and only Ge_3Mn_5 clusters and diluted Mn atoms coexist. The overall magnetic signal becomes comparable to the one measured on annealed samples in which only Ge_3Mn_5 clusters are observed by TEM [see Figs. 15(a) and 15(b)]. Ge_3Mn_5 clusters give a magnetic signal vanishing at 300 K, corresponding to the Curie temperature of bulk Ge_3Mn_5, while the diluted Mn atoms remaining in the Ge matrix give a paramagnetic signal that becomes negligible above 50 K, as shown in Fig. 15(a).

In conclusion, at low growth temperatures ($T_g \leq 120$ °C), the nanocolumns are made of almost four independent elongated magnetic nanostructures. For $T_g > 120$ °C, these independent nanostructures percolate into a single nanocolumn, sharply leading to higher blocking temperatures. Increasing
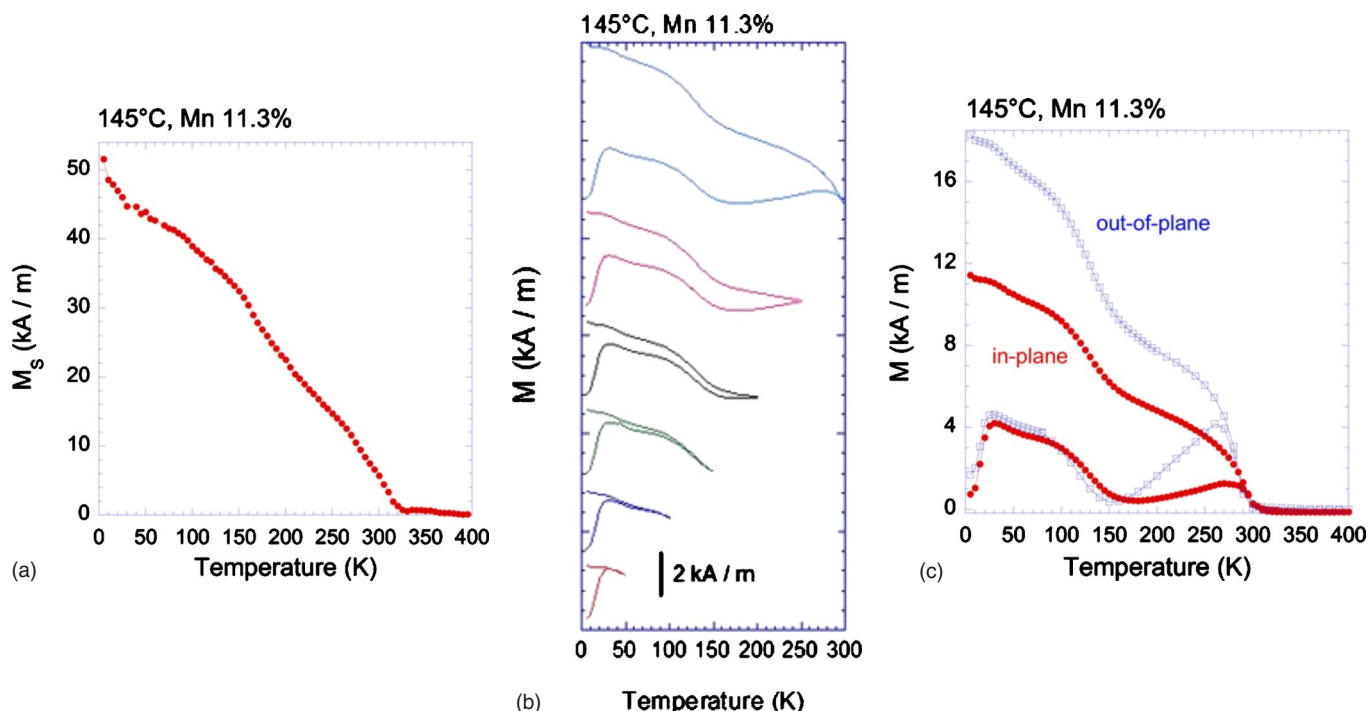
FIG. 13. (Color online) (a) Temperature dependence of the saturation magnetization of a $Ge_{0.89}Mn_{0.11}$ sample grown at 145 °C. The applied field is 2 T. (b) ZFC-FC measurements. The in-plane applied field is 0.015 T. Magnetization was recorded up to different T_0 temperatures: 50, 100, 150, 200, 250, and 300 K. Curves are shifted up for more clarity. (c) ZFC-FC curves for in-plane (red dots) and out-of-plane (open blue squares) applied fields (0.015 T).

T_g leads to larger columns with a wider size distribution, as evidenced by ZFC-FC measurements and given by TEM observations. In parallel, some Ge_3Mn_5 clusters start to form and their contribution increases on increasing T_g. The results on magnetic anisotropy seem counterintuitive. Indeed, Ge_3Mn_5 clusters exhibit strong out-of-plane anisotropy whereas nanocolumns, which are highly elongated magnetic structures, are almost isotropic. This effect is probably due to compensating in-plane magnetoelastic coupling (due to the column compression) and out-of-plane shape anisotropy.

V. CONCLUSION

In this paper, we have investigated the structural and magnetic properties of thin $Ge_{1-x}Mn_x$ films grown by low-temperature molecular beam epitaxy. A wide range of growth temperatures and Mn concentrations have been explored. All the samples contain Mn-rich nanocolumns as a consequence of 2D spinodal decomposition. However, their size, crystalline structure, and magnetic properties depend on growth temperature and Mn concentration. For low growth temperatures, the nanocolumns are very small (their diameter ranges between 1.8 nm for 1.3% of Mn and 2.8 nm for 11.3% of Mn), their Curie temperature is rather low (<170 K), and they behave almost as four uncorrelated superparamagnetic nanostructures. Increasing Mn concentration leads to higher column densities while the diameters remain nearly unchanged. For higher growth temperatures, the nanocolumn mean diameter increases and their size distribution widens. Moreover the four independent magnetic nanostructures per-

colate into a single magnetic nanocolumn. Some columns are ferromagnetic even if the Curie temperatures remain quite low. In this regime, increasing the Mn concentration leads to larger columns, while their density remains nearly the same. In parallel, Ge_3Mn_5 nanoclusters start to form in the film with their c axes perpendicular to the film plane. In both temperature regimes, the Mn incorporation mechanism in the nanocolumns and/or in the matrix changes above 5% of Mn and nanocolumns exhibit an isotropic magnetic behavior due to the competing effects of out-of-plane shape anisotropy and in-plane magnetoelastic coupling. Finally, for a narrow range of growth temperatures around 130 °C, the nanocolumns exhibit Curie temperatures higher than 400 K. The origin of ferromagnetism in these nanocolumns and the dependence of T_C on growth temperature remain at the moment unexplained. As for their crystalline structure, at low growth temperature, we can observe by TEM small, coherently strained nanocolumns. At 130 °C, the nanocolumns exhibit uniaxial relaxation, the which may be the cause of the high Curie temperature, and finally at higher growth temperature, the nanocolumns are mostly amorphous. We are currently using synchrotron-radiation-based techniques to investigate in detail the crystalline structure of nanocolumns for different growth temperatures. Moreover, a systematic chemical analysis using EFTEM as a function of growth temperature is also in progress. Indeed, the Mn concentration in the nanocolumns may change with T_g. Finally, $T_g=130$ °C appears as a singular temperature because Ge_3Mn_5 is likely to form and the Mn incorporation in the nanocolumns and/or the matrix is modified as shown in Sec. III. Our goal is now to probe the crystalline structure inside the nanocolumns, in particular the
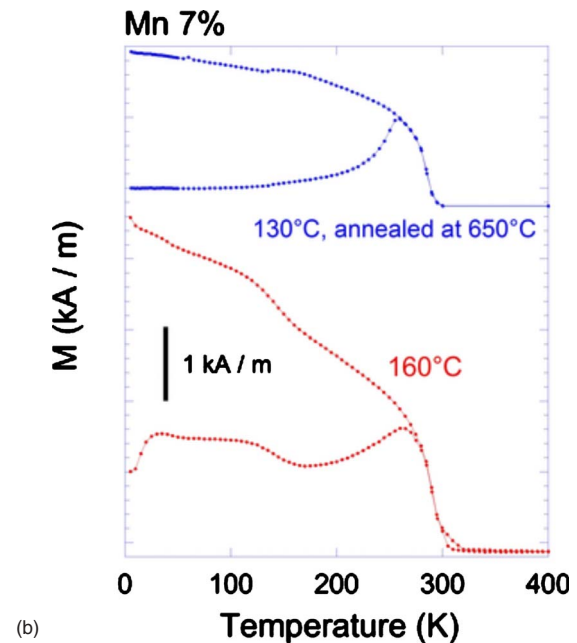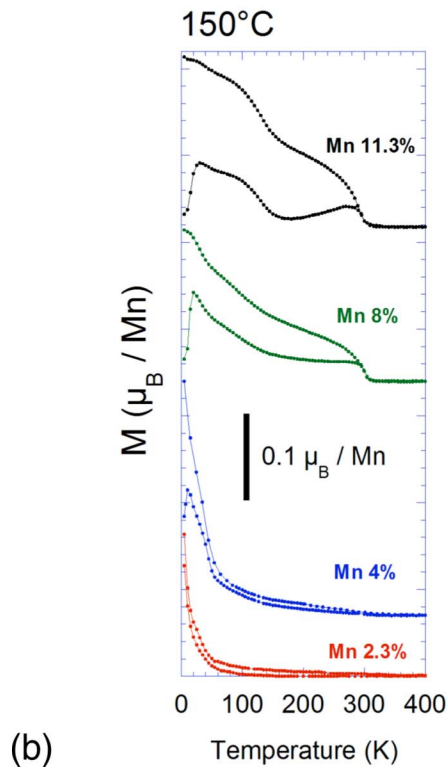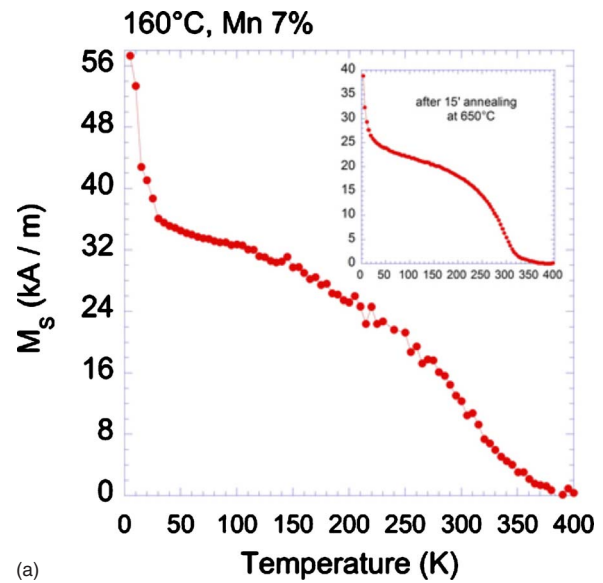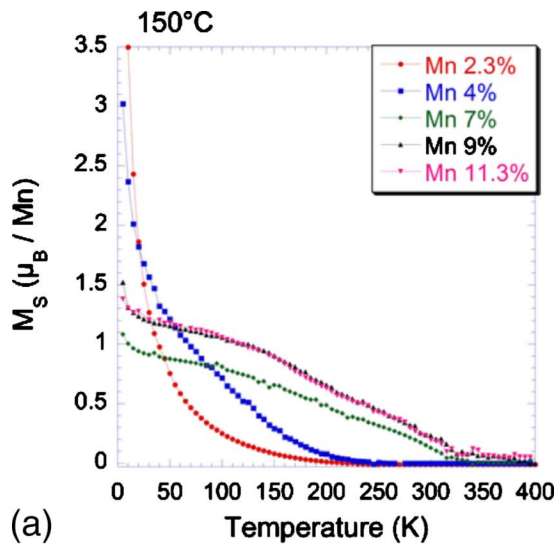
FIG. 14. (Color online) (a) Temperature dependence of the saturation magnetization (in μ_B/Mn) of $Ge_{1-x}Mn_x$ films grown at 150 °C plotted for different Mn concentrations 2.3, 4, 7, 9, and 11.3%. (b) ZFC-FC measurements performed on $Ge_{1-x}Mn_x$ films grown at 150 °C. The in-plane applied field is 0.025 T for 2.3% and 4% and 0.015 T for 8% and 11.3%.

FIG. 15. (Color online) (a) Temperature dependence of the saturation magnetization (in kA/m) of a $Ge_{0.93}Mn_{0.07}$ sample grown at 160 °C. The inset shows the temperature dependence of a sample grown at 130 °C and annealed at 650 °C for 15 min. After annealing, the magnetic signal mostly arises from Ge_3Mn_5 clusters. (b) Corresponding ZFC-FC measurements. The in-plane applied field is 0.015 T.

position of Mn atoms in the distorted diamond structure, using highly selective techniques, which is essential to understand magnetic and transport properties in $Ge_{1-x}Mn_x$ films.

ACKNOWLEDGMENTS

*thibaut.devillers@cea.fr

†matthieu.jamet@cea.fr

[1] H. Ohno, D. Chiba, F. Matsukura, T. Omiya, E. Abe, T. Dietl, Y. Ohno, and K. Ohtani, Nature (London) **408**, 944 (2000).

[2] H. Boukari, P. Kossacki, M. Bertolini, D. Ferrand, J. Cibert, S. Tatarenko, A. Wasiela, J. A. Gaj, and T. Dietl, Phys. Rev. Lett. **88**, 207204 (2002).

[3] T. Dietl, Semicond. Sci. Technol. **17**, 377 (2002).

[4] T. Dietl, Nat. Mater. **5**, 673 (2006).

[5] T. Fukushima, K. Sato, H. Katayama-Yoshida, and P. H. Dederichs, Jpn. J. Appl. Phys., Part 2 **45**, L416 (2006).

[6] Y. D. Park, A. T. Hanbicki, S. C. Erwin, C. S. Hellberg, J. M. Sullivan, J. E. Mattson, T. F. Ambrose, A. Wilson, G. Spanos, and B. T. Jonker, Science **295**, 651 (2002).

[7] N. Pinto, L. Morresi, M. Ficcadenti, R. Murri, F. D'Orazio, F. Lucari, L. Boarino, and G. Amato, Phys. Rev. B **72**, 165203 (2005).

[8] A. P. Li, J. F. Wendelken, L. C. Feldman, J. R. Thompson, and H. H. Weitering, Appl. Phys. Lett. **86**, 152507 (2005).

[9] F. Tsui, L. He, L. Ma, A. Tkachuk, Y. S. Chu, K. Nakajima, and T. Chikyow, Phys. Rev. Lett. **91**, 177203 (2003).

[10] S. Cho, S. Choi, S. C. Hong, Y. Kim, J. B. Ketterson, B.-J. Kim, Y. C. Kim, and J. H. Jung, Phys. Rev. B **66**, 033303 (2002).

[11] J.-S. Kang *et al.*, Phys. Rev. Lett. **94**, 147202 (2005).

[12] C. Bihler, C. Jaeger, T. Vallaitis, M. Gjukic, M. S. Brandt, E. Pippel, J. Woltersdorf, and U. Gösele, Appl. Phys. Lett. **88**,

112506 (2006).

[13] L. Morresi, J. Ayoub, N. Pinto, M. Ficcadenti, R. Murri, A. Ronda, and I. Berbezier, Mater. Sci. Semicond. Process. **9**, 836 (2006).

[14] M. Passacantando, L. Ottaviano, F. D'Orazio, F. Lucari, M. D. DeBiase, G. Impellizzeri, and F. Priolo, Phys. Rev. B **73**, 195207 (2006).

[15] S. Ahlers, D. Bougeard, N. Sircar, G. Abstreiter, A. Trampert, M. Opel, and R. Gross, Phys. Rev. B **74**, 214411 (2006).

[16] T. B. Massalski, *Binary Alloy Phase Diagrams* (American Society for Metals, Metals Park, OH, 1990), Vol. 2.

[17] Y. D. Park, A. Wilson, A. T. Hanbicki, J. E. Mattson, T. Ambrose, G. Spanos, and B. T. Jonker, Appl. Phys. Lett. **78**, 2739 (2001).

[18] S. Sugahara, K. L. Lee, S. Yada, and M. Tanaka, Jpn. J. Appl. Phys., Part 1 **44**, 1426 (2005).

[19] M. Jamet, A. Barski, T. Devillers, V. Poydenot, R. Dujardin, P. Bayle-Guillemaud, J. Rothman, E. Bellet-Amalric, A. Marty, J. Cibert, R. Mattana, and S. Tatarenko, Nat. Mater. **5**, 653 (2006).

[20] S. Kagawa, T. Mikawa, and T. Kaneda, Jpn. J. Appl. Phys., Part 1 **21**, 1616 (1982).

[21] J. B. Forsyth and P. J. Brown, J. Phys.: Condens. Matter **2**, 2713 (1990).

[22] R. W. Chantrell, N. Walmsley, J. Gore, and M. Maylin, Phys. Rev. B **63**, 024410 (2000).

[23] O. Fruchart, P.-O. Jubert, C. Meyer, M. Klaua, J. Barthel, and J. Kirschner, J. Magn. Magn. Mater. **239**, 224 (2002).